

# A STUDY OF CH AND REDDENING IN THE DIFFUSE MOLECULAR CLOUD

MBM40

by

BRETT MEERDINK

(Under the Direction of Loris Magnani)

## ABSTRACT

The existence of dark molecular gas, signifying molecular gas in interstellar clouds that is difficult or impossible to detect by spectroscopic emission lines, makes mass determination of small, diffuse molecular clouds difficult. The current thinking is that more sensitive observations of CO(1-0), or OH at 18 cm, or CH at 9 cm, may detect most of the dark molecular gas. We use archival CH observations of the 3335 MHz lines in the high-latitude molecular cloud, MBM 40, to address this issue. By averaging several nearby positions from the original CH observations, we produce a new, more sensitive, CH data set to trace molecular hydrogen in its lowest density component. We found a significantly higher molecular mass for MBM 40 ( $[44 \pm 22]$  Solar Masses; about a factor of 2 greater than previous work) which indicates that at least some of the dark molecular gas in this cloud is detectable with sensitive CH observations.

INDEX WORDS: ISM: clouds, ISM: molecules, MBM40

A STUDY OF CH AND REDDENING IN THE DIFFUSE MOLECULAR CLOUD  
MBM40

by

BRETT MEERDINK

B.S., The State University of New York at Oswego, 2020

A Thesis Submitted to the Graduate Faculty  
of The University of Georgia in Partial Fulfillment  
of the  
Requirements for the Degree

MASTER OF SCIENCE

ATHENS, GEORGIA

2023

© 2023

Brett Meerdink

All Rights Reserved

A STUDY OF CH AND REDDENING IN THE DIFFUSE MOLECULAR CLOUD  
MBM40

by

BRETT MEERDINK

Approved:

Major Professor: Loris Magnani

Committee: Jean-Pierre Caillault  
Robin Shelton

Electronic Version Approved:

Ron Walcott  
Dean of the Graduate School  
The University of Georgia  
May 2023

## DEDICATION

To my father, in loving memory

## ACKNOWLEDGMENTS

I would like to thank Loris Magnani, Jean-Pierre Caillault, and Robin Shelton for taking the time to be on my graduate committee and giving me feedback on my thesis.

I would especially like to thank Loris for the time he spend mentoring me, the opportunity he gave me to do Astronomy research, and him showing me the light (radio waves) from diffuse gas in space.

I would like to thank Ray Chastain for letting me use two figures from his thesis.

And I would like to thank my Mom, Dad, and sister for their love and support throughout my academic journey, which is far from over.

## TABLE OF CONTENTS

	Page
ACKNOWLEDGMENTS . . . . .	v
LIST OF FIGURES . . . . .	viii
LIST OF TABLES . . . . .	x
 CHAPTER	
1 MOLECULAR CLOUDS AND HOW WE OBSERVE THEM . . . . .	1
2 THE PROBLEM OF DARK GAS AND TRACING MOLECULAR GAS AT THE LOWEST EXTINCTIONS AND COLOR EXCESSES . . . . .	5
3 ARECIBO CH DATA AND ANALYSIS . . . . .	8
3.1 THE DIFFUSE MOLECULAR CLOUD MBM 40 . . . . .	8
3.2 ORIGINAL DATA . . . . .	8
3.3 SUMMED SPECTRA . . . . .	10
4 THE CH - E(B-V) RELATION . . . . .	23
4.1 INTRODUCTION . . . . .	23
4.2 THE W(CH) - E(B-V) DATA . . . . .	24
4.3 HOW TO CALCULATE N(H <sub>2</sub> ) FROM W(CH) . . . . .	31
4.4 FINDING N(H <sub>2</sub> ) THROUGHOUT MBM 40 . . . . .	31

4.5	THE MOLECULAR EXTENT OF MBM 40 . . . . .	34
4.6	ERROR ANALYSIS INCLUDING THE $\frac{W(\text{CH})}{E(\text{B-V})}$ RELATION . . .	35
5	THE MASS OF MBM 40 FROM SENSITIVE CH OBSERVATIONS. . .	37
5.1	DETERMINATION OF CLOUD MASS . . . . .	37
5.2	DISCUSSION . . . . .	39
6	CONCLUSIONS . . . . .	41
	BIBLIOGRAPHY . . . . .	42

## LIST OF FIGURES

3.1	CO(1-0) map of MBM 40 originally published in Chastain (2005). The color bar shows a gradient used in the figure corresponding to the velocity-integrated CO (1-0) antenna temperature. . . . .	11
3.2	Original position grid first published in Chastain (2005). The small circles denote the 164 positions where the CH 3335 MHz line was observed using the Arecibo telescope. The filled-in circles represent CH detections according to Chastain (2005). The larger circles represent CH observations with the old NRAO 43-m telescope (see Magnani et al. 1998). . . . .	12
3.3	Grid containing location (Right Ascension and Declination in degrees) of the old and new CH data positions. The average of the old positions is shown in orange in-between the old positions (shown in yellow). . .	13
3.4	MBM 40 CH spectra corresponding to the positions 1-6 in figure 3.3 .	15
3.5	MBM 40 CH spectra corresponding to the positions 7-12 in figure 3.3	16
3.6	MBM 40 CH spectra corresponding to the positions 13-18 in figure 3.3	17
3.7	MBM 40 CH spectra corresponding to the positions 19-24 in figure 3.3	18
3.8	MBM 40 CH spectra corresponding to the positions 25-30 in figure 3.3	19
3.9	MBM 40 CH spectra corresponding to the positions 31-36 in figure 3.3	20
3.10	MBM 40 CH spectra corresponding to the positions 36-41 in figure 3.3	21

3.11	MBM 40 CH spectra corresponding to the positions 40-47 in figure 3.3	22
4.1	Plot of $W^*(CH)$ (using $T_A$ instead of $T_B$ ) as a function of $A_v$ . The slope of the relation is $(0.31 \pm 0.05) \text{ K km s}^{-1} \text{ mags}^{-1}$ with a P value of $4.35 \times 10^{-8}$ . Representative error bars are shown for one of the points.	30
4.2	A $2^\circ \times 2^\circ$ reddening map of MBM 40 from Schlegel, Finkbeiner and Davis (1998) using galactic coordinates. The reddening map is 100 by 100 pixels centered at (37.6, 44.7). A color excess value ( $E(V-B)$ ) at each point in the map corresponds to a value on the colorbar. . . . .	32
4.3	Bins corresponding to $E(V-B)$ values in MBM 40 from the color excess map in figure 4.2 . . . . .	33

LIST OF TABLES

4.1 MBM40 CH 3335 MHz Detections and Reddening Values . . . . . 26

4.2 Tabulated data derived from the reddening map of MBM 40 in figure 4.2. The color excess values at each point are placed into bins spanning a color excess range with a total number of points in each bin is given by variable N. The triple underline denotes the boundary between the color excess bins which correspond to the lowest-density molecular component of MBM 40 and those that are likely to be mostly atomic. 36

5.1 Color excess range and associated masses. The triple underline denotes the color excess range which corresponds to the lowest-density molecular component of MBM 40. . . . . 39

## CHAPTER 1

### MOLECULAR CLOUDS AND HOW WE OBSERVE THEM

The interstellar medium, the “stuff” between the stars, is a great reservoir of gas and dust and an important part of our galaxy. The Milky Way is estimated to contain  $10^{10}$  solar masses of gas and  $10^8$  solar masses of dust. Much of the gas in spiral galaxies like the Milky Way is in interstellar molecular clouds - clouds of mostly gravitationally bound gas and dust spanning parsecs in size and with masses as high as  $10^5 - 10^6$  solar masses. The clouds are composed primarily of molecular hydrogen,  $\text{H}_2$ , and atomic helium, with other molecular species present in trace amounts. They are formed from extended cold atomic gas regions and evolve and form stars as galaxies cycle through the star-gas cycle (see, e.g., Magnani and Shore 2017). Molecular clouds also contain large amounts of dust and are sometimes classified by their average extinction<sup>1</sup> with Giant Molecular Clouds and the smaller dark molecular clouds having regions with the highest extinction while diffuse molecular clouds can have extinctions as low as a few tenths of a magnitude. Molecular clouds can also be categorized by mass. Giant Molecular Clouds range from  $10^4 - 10^6$  solar masses while the smaller clouds have masses from  $0.1 - 10^3$  solar masses. These two criteria can be combined in the case of the smaller clouds: diffuse molecular clouds are

---

<sup>1</sup>Interstellar extinction is the absorption along a line of sight produced by the summative effects of scattering and absorption of background starlight.

defined as those with visual extinction,  $A_V$ , less than 1 mag, translucent clouds have  $1 \leq A_V \leq 5$  mags, and dark clouds have at least one region with  $A_V > 5$  mags. It is understood that even dark clouds can have substantially large regions with  $A_V < 5$ , usually in their outer regions.

The chemistry of molecular clouds is a rich and complex study (e.g., Hartquist 1990). In diffuse molecular clouds, diatomic molecules are the most abundant and easily observed molecules. The most abundant and important molecule is  $H_2$  followed by CO with the CO- $H_2$  abundance ranging from  $10^{-6}$  to  $10^{-4}$  in clouds with molecular hydrogen column densities ( $N(H_2)$ ) greater than  $10^{19} \text{ cm}^{-2}$ . The question of what is a molecular interstellar cloud versus an atomic cloud is difficult and somewhat subjective (see Magnani and Shore 2017). We will consider an observational definition: molecular clouds are those regions where the lowest rotational transition of CO can be readily observed by millimeter radio telescopes.

In addition to CO, the free radicals OH and CH are also abundant ( $\frac{OH}{H_2} \sim 10^{-7}$  and  $\frac{CH}{H_2} \sim 10^{-8}$ ) and have hyperfine transitions of the lowest rotational state which make them relatively easy to observe using ground-based radio telescopes. Under normal conditions free radicals are highly reactive; however, in the interstellar medium, they are stable because of the very low densities ( $n \sim 10^2 - 10^3 \text{ cm}^{-3}$ ). These molecules have fine-structure transitions leading to emission lines in the centimeter part of the spectrum (18 cm for OH, 9 cm for CH) and can be used as tracers of molecular hydrogen.

Studies of molecular clouds have primarily used the lowest CO rotational transitions in the millimeter portion of the radio spectrum to trace molecular hydrogen.

This is due to the difficulty in detecting the rotational transitions of  $\text{H}_2$  from the ground. Problems may arise using CO as a tracer due to the variability of the CO –  $\text{H}_2$  ratio across diffuse molecular clouds due to the photo-dissociation of CO varying throughout the cloud (see, e.g., Magnani and Shore 2017). For nearly 4 decades, radio astronomers who studied molecular clouds considered CO(1-0) observations as a way to detect most of the molecular material in an interstellar cloud.

In a controversial paper, Grenier et al. (2005) proposed that CO surveys may not trace as much as half of the molecular gas in the interstellar medium. Using gamma rays to trace molecular hydrogen throughout the sky, away from the Galactic plane they found double the amount of molecular hydrogen as predicted by previous CO observations. They referred to this spectroscopically unobserved gas as “dark gas” (also referred to as “dark molecular gas”: see Wolfire, Hollenbach and McKee 2010), although this gas is in no way associated with dark matter. Subsequent work (e.g., Donate and Magnani 2017; Donate, White, and Magnani 2019) has shown that a good portion of the dark molecular gas can be detected spectroscopically with more sensitive observations than are usually made.

In this thesis, we will examine whether or not a substantial amount of dark molecular gas is present in the diffuse high-latitude cloud MBM 40. The layout of this thesis follows: in chapter 2 we discuss the problem of dark gas and tracing molecular gas at the lowest extinction and color excess; in chapter 3 we discuss the archival Arecibo MBM 40 CH data and our analysis of it. Briefly, we sum up the spectra from adjacent positions to produce a new spectral data set with higher sensitivity. In chapter 4 we discuss how our new CH spectra can be used to determine the spectral

extent of the molecular portion of MBM 40 and how color-excess values throughout MBM 40 relate to the CH and H<sub>2</sub> column densities. In chapter 5 we discuss how to derive the mass of MBM 40 from our data and we compare our results with CO estimates of the molecular cloud mass. In chapter 6 we discuss our results and the efficacy of CH 9 cm observations for determining the dark molecular gas content of diffuse clouds.

## CHAPTER 2

### THE PROBLEM OF DARK GAS AND TRACING MOLECULAR GAS AT THE LOWEST EXTINCTIONS AND COLOR EXCESSES

”Dark gas” was originally used to describe molecular gas that could not be traced by spectroscopic methods. Coined by Greiner et al. (2005), they proposed that as much as half of the molecular gas in the interstellar medium could not be traced by CO (1-0) observations. For more than five decades, CO observations at 115 GHz have been the principal way by which our knowledge of molecular clouds has come about (e.g., Heyer and Dame 2015). However, Grenier et al. (2005) used gamma rays and infrared data to trace molecular hydrogen in several regions and found twice as much molecular hydrogen as traced by previous CO surveys of those regions. However, the CO surveys Grenier et al. used were not particularly sensitive. Deeper integrations of the CO(1-0) transitions can frequently uncover extended, low-density molecular envelopes surrounding diffuse molecular clouds (e.g., Cotten and Magnani 2013). Thus, Donate and Magnani (2017) found that increasing the CO integration time by factors of 3-4 compared to typical surveys revealed the presence of weak spectral lines and decreased the amount of dark gas in a diffuse cloud by a factor of 2. This indicates that a significant portion of the dark molecular gas could be traced

by spectroscopy of molecular tracers by increasing the integration time and thus the sensitivity of the observations.

Traditionally, the best molecular tracers of low density ( $10^2 - 10^3 \text{ cm}^3$ ) molecular gas in low-extinction regions have been the CO(1-0) transition at 115 GHz, the two main lines of OH at 1665 and 1667 MHz, the CH main line at 3335 MHz, and perhaps the C<sub>3</sub>H<sub>2</sub> transitions at 18.3 GHz (Cox, Güsten, and Henkel 1988; Peng et al 1992) and the H<sub>2</sub>CO hyperfine transition at 4.8 GHz (Magnani and Shore 2017). In an effort to determine the efficacy of OH as a tracer of dark molecular gas, Donate, White, and Magnani (2019) made observations of the OH 1.6 GHz lines in a diffuse molecular cloud and found that while the OH distribution was not as extended as the CO, the high sensitivity observations showed about as much dark gas as the CO observations. For similar fairly long integration times ( $\sim 0.5$  hours), both the CO(1-0) line and the 1667 MHz OH line (which is typically stronger than the 1665 MHz line by a factor of 2) are effective tracers of at least some dark molecular gas.

Another promising molecular tracer is the radical CH. CH has a hyperfine structure transition in its ground rotational state, the 3335 MHz emission line, which is detectable using radio telescopes. One survey of this emission line along the galactic plane survey was conducted by Lars E.B. Johansson during the latter part of the 1970s using the 26 m radiotelescope at the Onsala Observatory (Johansson 1979). They found the molecular distribution of CH is more extended than the distribution revealed by CO(1-0) surveys and the CH distribution is between that of CO and HI as mapped via the 21 cm line. The CH distribution has a peak at the molecular ring of the Galaxy and does not decrease as sharply as the CO emission. However,

there were no follow-up studies due to the difficulty in observing the CH 3.3 GHz line because of the lack of upper S-band receivers and the substantial amount of integration time required to detect it.

Other studies have also shown that CH can be used to trace molecular gas on smaller scales where CO has not been detected (e.g., Magnani and Onello 1993; Federman and Wilson 1984; Sandell et al. 1987). However, as with dark molecular gas, it is always challenging to determine whether a particular tracer or method for detecting molecular gas is advantageous over CO(1-0) observations since the latter are often not particularly sensitive. Numerous CO studies or surveys focus on the detection of the most prominent molecular emission regions where star formation occurs and are often uninterested in the detection of low-density molecular envelopes. However, if one wants to study the interface between the atomic medium and the molecular cloud in an effort to study how diffuse molecular clouds are formed, then studies of the low density envelopes are crucial.

Integration times more than 30 minutes with a rms  $1-\sigma$  noise levels  $< 20$  mK can result in extended emission exhibited by the CO(1-0) line. Nonetheless, it is reasonable to say CH 3335 MHz observations can be used to trace low-density envelopes in diffuse and translucent molecular clouds (see, e.g. Magnani and Onello 1993). Another such study of CH on a smaller scale was conducted by Chastain (2005) who studied the CH distribution in MBM 40. Next, we discuss the structure of the diffuse interstellar cloud MBM 40, the MBM 40 CH data used by Chastain (2005), and their comparison of MBM 40 CH and CO data.

## CHAPTER 3

### ARECIBO CH DATA AND ANALYSIS

#### 3.1 THE DIFFUSE MOLECULAR CLOUD MBM 40

MBM 40 is a diffuse high-latitude molecular cloud located at ( $l \sim 35^\circ$ ,  $b \sim 45^\circ$ ). Figure 3.1 is a CO (J=1-0) map of MBM 40 from Chastain (2005) at  $\sim 50''$  resolution. The lowest contour represents a velocity integrated antenna temperature level of  $\sim 1 \text{ K km s}^{-1}$ , but CO emission extends to  $W(\text{CO}) < 1 \text{ K km s}^{-1}$  because the rms of the Chastain map is only about 0.7 K in antenna temperature, thus only the most molecular prominent features appear. The densest portion of the cloud is in the shape of an arc with a main ridge to the west connected to a secondary ridge to the east. A lower density molecular “envelope” surrounds the arc and has been detected in CO (Cotten and Magnani 2013) and OH (Cotten et al. 2012). The distance to the cloud has been established to be  $93 \pm 20 \text{ pc}$  (Zucker et al. 2019). We will discuss the mass estimates for this object in chapter 5. For more details about MBM 40 see Magnani et al. (1996).

#### 3.2 ORIGINAL DATA

The original CH data for MBM 40 was collected by Ray Chastain in 2003-4 using the Arecibo radio telescope. The Arecibo radio telescope was a 305-meter spher-

ical reflecting dish that was built near Arecibo, Puerto Rico. At the time the data were taken, the receivers were housed in a three-story building suspended above the reflector using a Gregorian system to correct for the spherical aberration of the dish. The receiver used for observations was a S-band High receiver which had 30 K system temperature on the sky. Details of how the telescope worked can be found in papers by Magnani (1993) and Goldsmith et al. (1995). The data for this project were collected as part of Arecibo astronomy projects A1708 and A1853 and were published by Chastain, Cotten, and Magnani (2010). In the original paper, 164 positions were observed in the diffuse molecular cloud MBM 40. (See Figure 3.2)

The spectrograph for the observations was the Interim Arecibo autocorrelator divided into four segments: two for each polarization of the main line at a frequency of 3335 MHz, and the remaining two for an upper satellite line at a frequency at 3349 MHz, and a lower satellite line frequency at 3264 MHz. Each autocorrelator section consisted of 1024 channels spanning a bandwidth of 800 MHz equivalent to a velocity range spanning  $70 \text{ km s}^{-1}$ . The resolution per channel was 0.781 kHz equivalent to  $.0703 \text{ km s}^{-1}$  per channel. There were several scans for each position in figure 3.2 with a minimum of 15 minutes spent per point resulting in a typical rms of 25 mK (Chastain 2005).

### 3.2.1 RADIOMETER EQUATION

We improved the sensitivity of the observations without taking new data, using the following logic: the radiometer equation given by equation 3.1 describes the one-sigma noise fluctuations in the antenna temperature,  $T_{\text{rms}}$  in a radio frequency spectrum.

This equation governs the noise from the Arecibo backend and is dependent on system temperature,  $T_{sys}$ , the width of each channel,  $\Delta\nu$ , and the integration time  $t$ .

$$T_{rms} = \frac{T_{sys}}{\sqrt{\Delta\nu \times t}} \quad (3.1)$$

The system noise can be decreased by increasing integration times or by using broader channels in frequency. By adding both dual main line polarizations, adding multiple scans for each position together, and by adding multiple nearby positions as shown in figure 3.3, the rms noise of the Arecibo data was decreased and the signal to noise ratio of any CH signal was increased. These new average positions are shown with orange labels in figure 3.3 which are centered between the old positions with yellow labels. By using this technique of adding adjacent spectra, we are improving the rms at the expense of the resolution. In this thesis, we intend to search for widespread low-density molecular emission, especially in regions of MBM 40 where Chastain 2005 found no molecular emission (see figure 3.2). Thus, the tradeoff between resolution and sensitivity is justified.

### 3.3 SUMMED SPECTRA

Figure 3.3 shows the pattern of positions that were summed to create the final, higher-sensitivity CH spectra. The summed spectra were then calibrated and fit with a polynomial baseline, which was removed. The individual spectra for the summed positions are shown in figures 3.4-3.11. The average  $1-\sigma$  rms levels of the spectral were  $\sim 14$  mK which is an improvement of nearly a factor of 2 from Chastain (2005). With this new dataset, we are now in a position to determine a mass for MBM 40

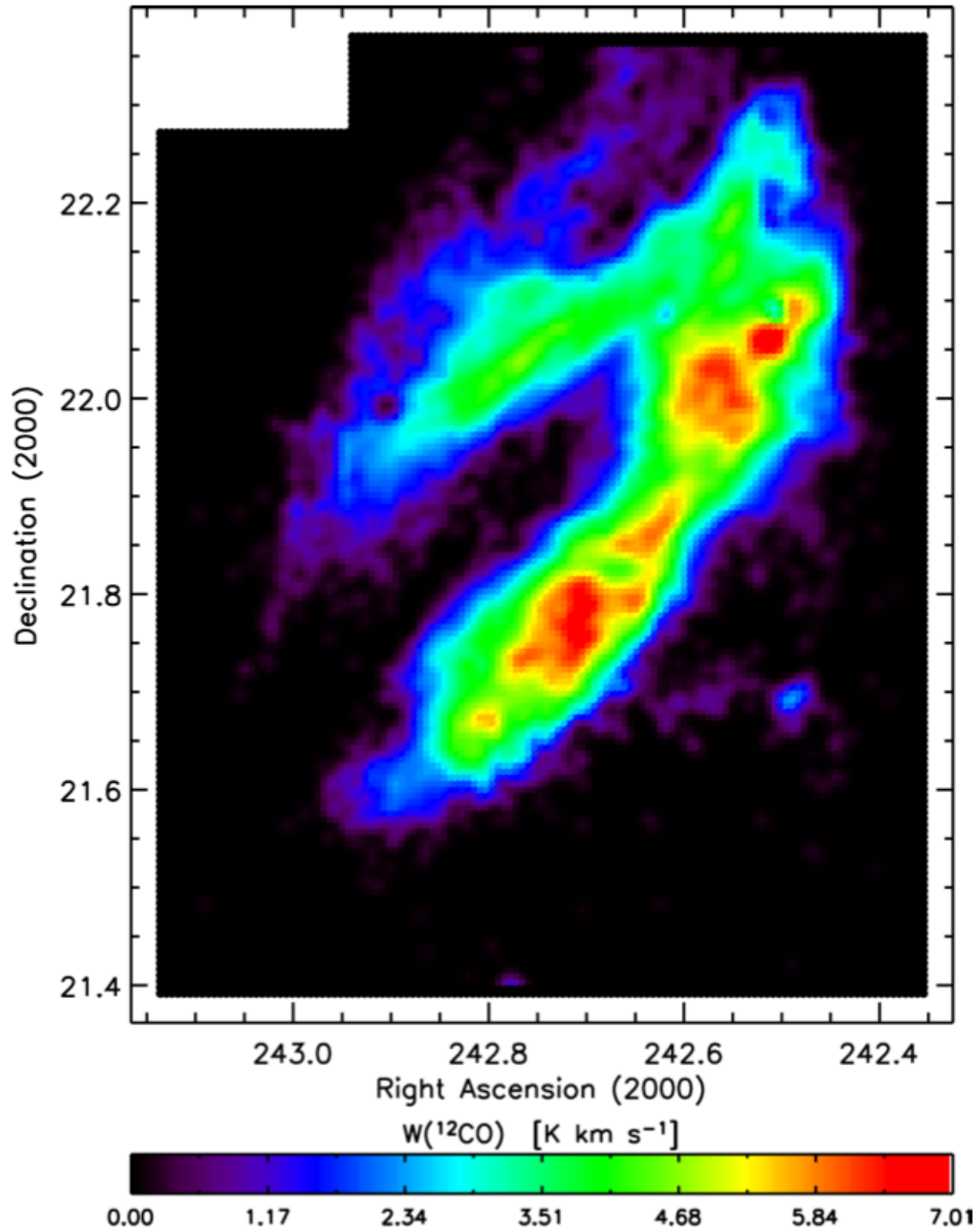


Figure 3.1: CO(1-0) map of MBM 40 originally published in Chastain (2005). The color bar shows a gradient used in the figure corresponding to the velocity-integrated CO (1-0) antenna temperature.

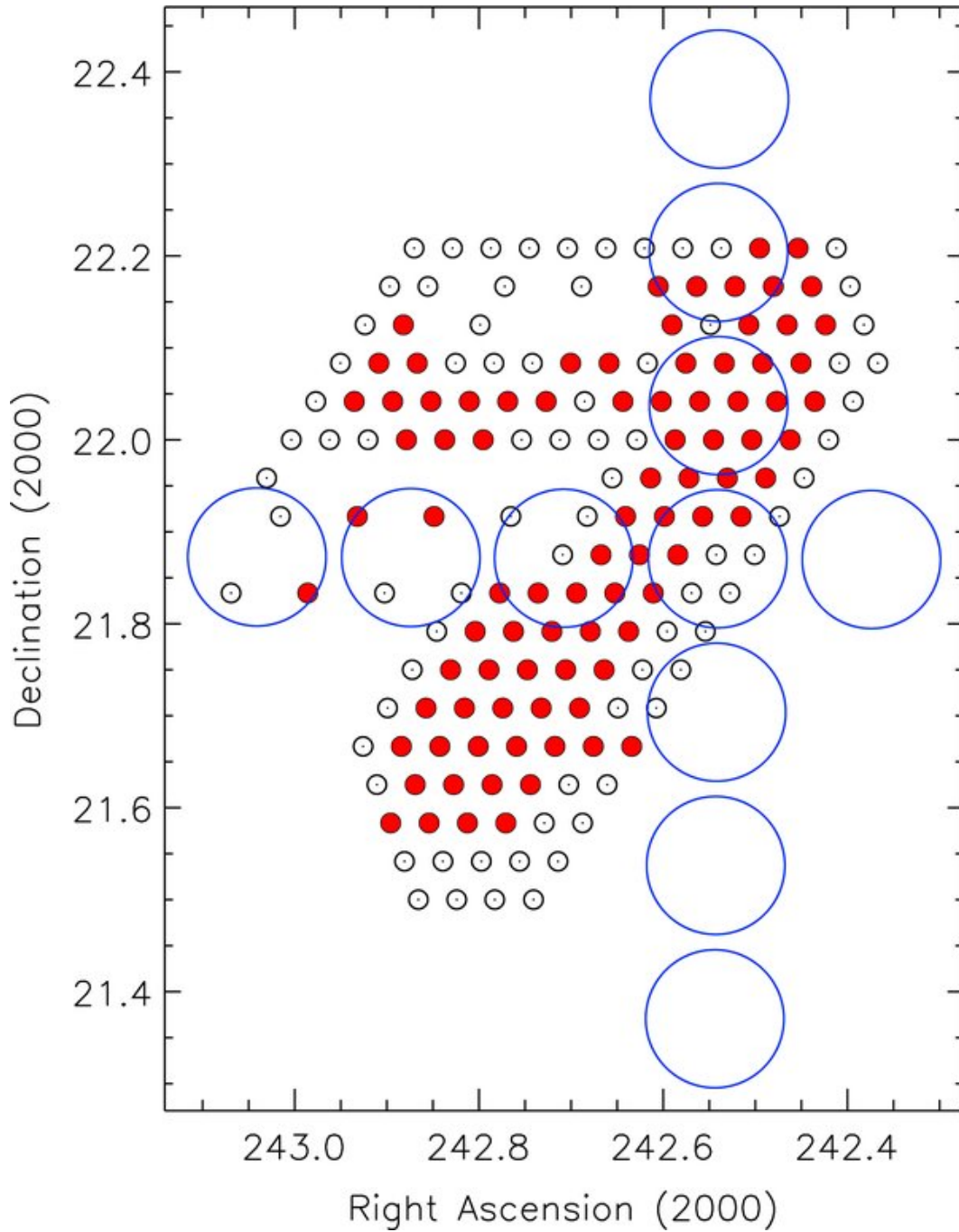


Figure 3.2: Original position grid first published in Chastain (2005). The small circles denote the 164 positions where the CH 3335 MHz line was observed using the Arecibo telescope. The filled-in circles represent CH detections according to Chastain (2005). The larger circles represent CH observations with the old NRAO 43-m telescope (see Magnani et al. 1998).

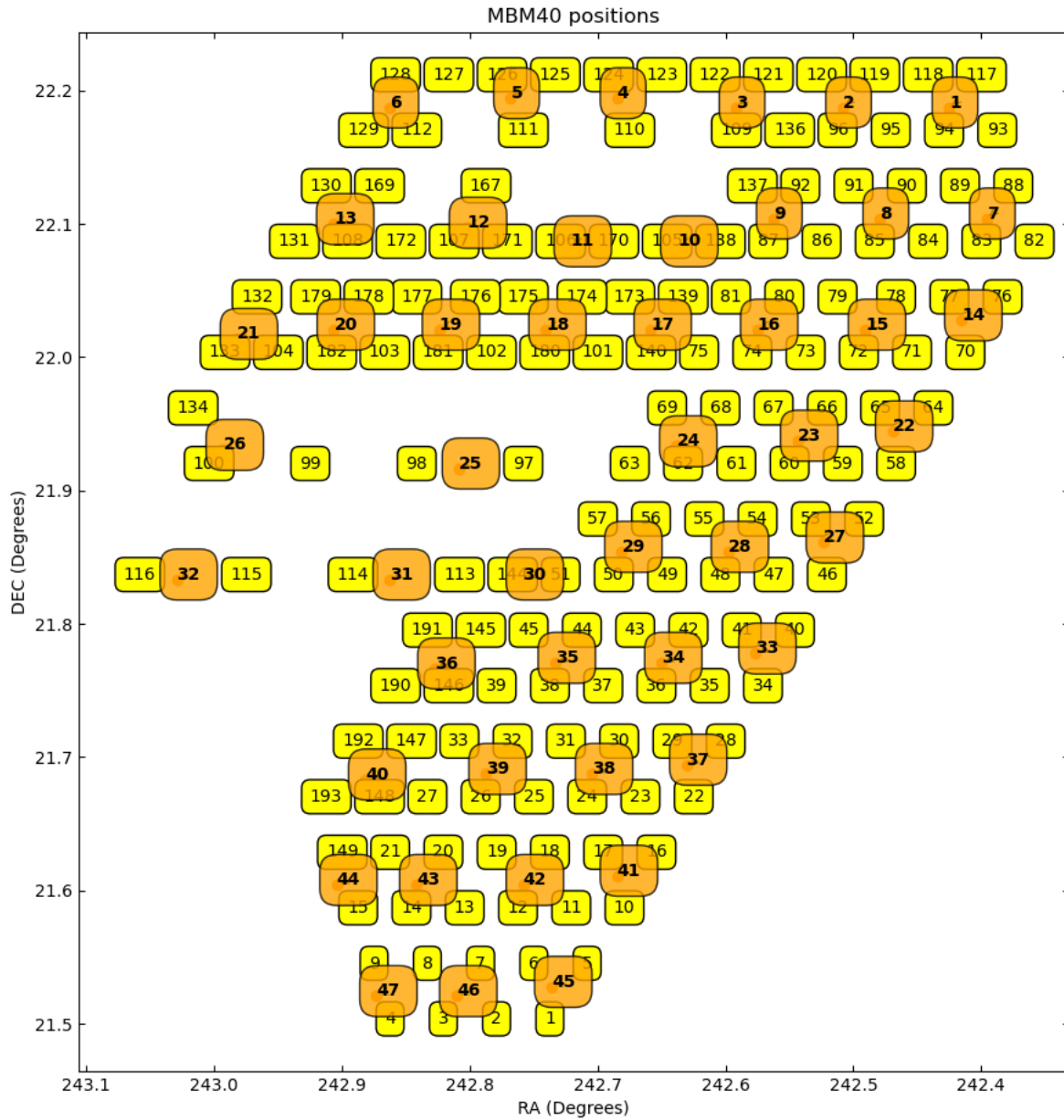


Figure 3.3: Grid containing location (Right Ascension and Declination in degrees) of the old and new CH data positions. The average of the old positions is shown in orange in-between the old positions (shown in yellow).

including the extended-low density molecular component. We note that by adding spectra from adjacent positions together, we detected CH at every sampled position (see figures 3.4-3.11). This is a notable improvement from the detection rate noted by Chastain (2005): 88 out of 164 and indicates that widespread CH emission is present in the cloud beyond the arc detected by Chastain (2005). Thus, sensitive CH observations of the 3335 MHz line are as effective at showing the molecular envelope of MBM 40 as the CO(1-0) and OH observations made by Cotten and Magnani (2013) and Cotten et al. (2012).

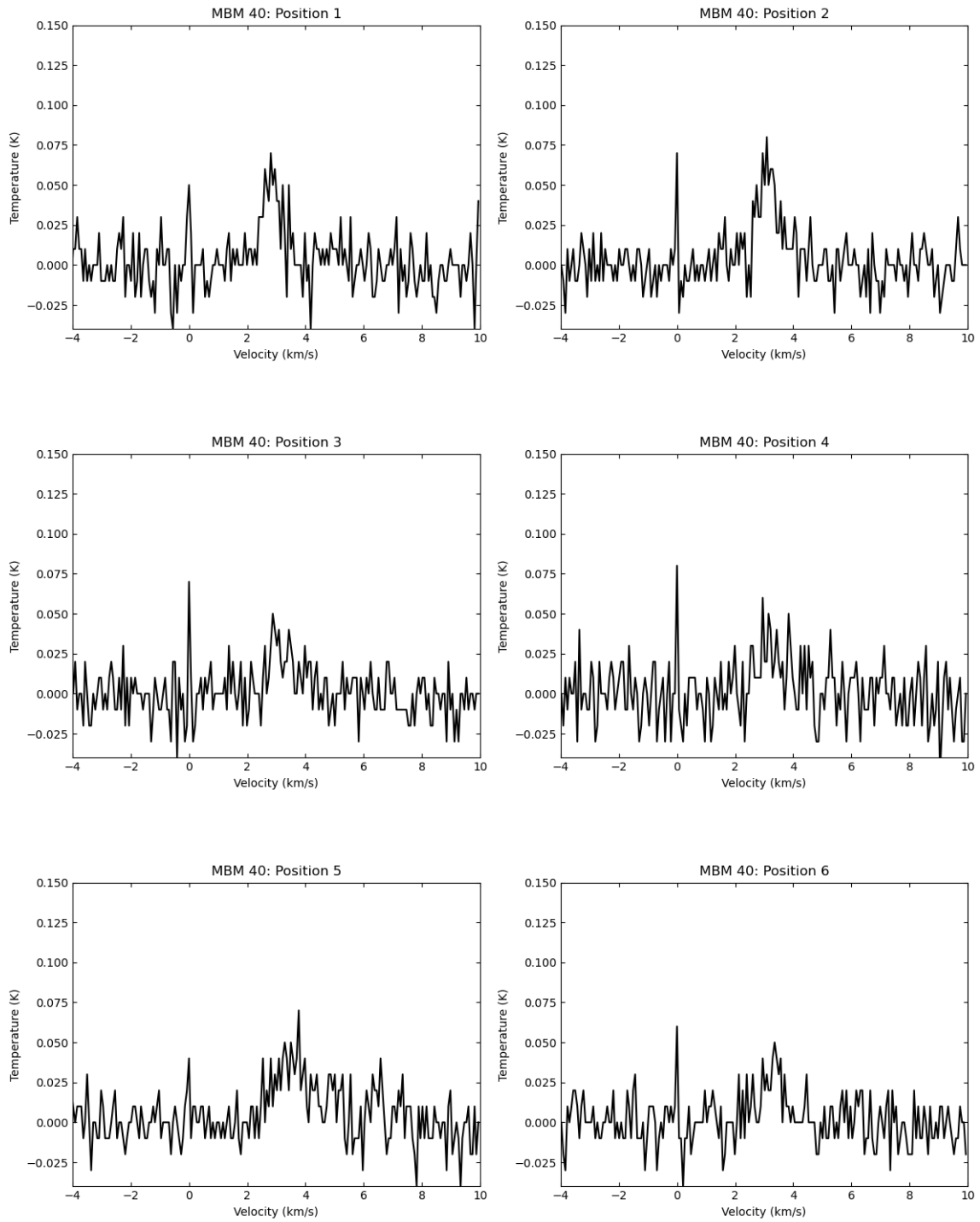


Figure 3.4: MBM 40 CH spectra corresponding to the positions 1-6 in figure 3.3

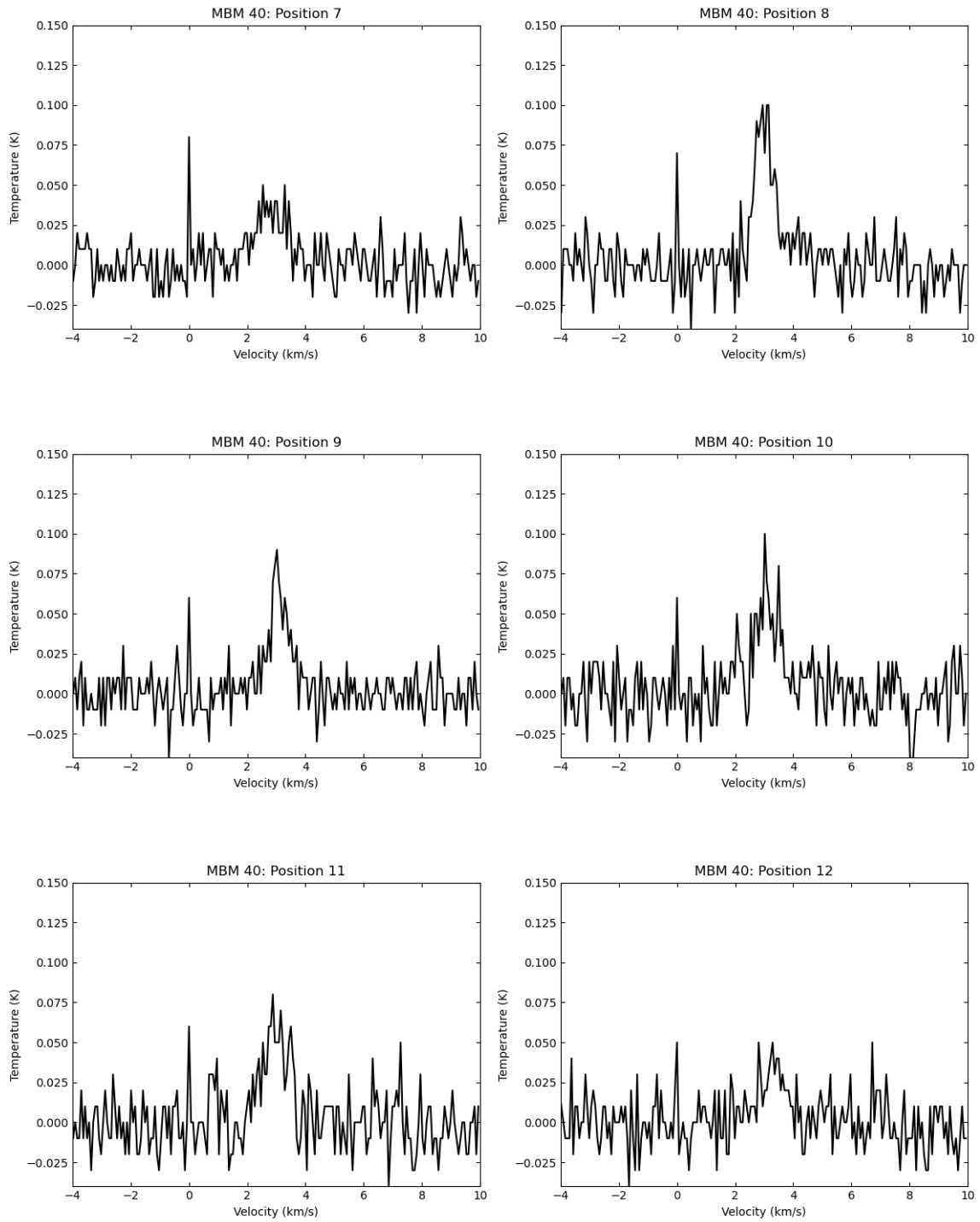


Figure 3.5: MBM 40 CH spectra corresponding to the positions 7-12 in figure 3.3

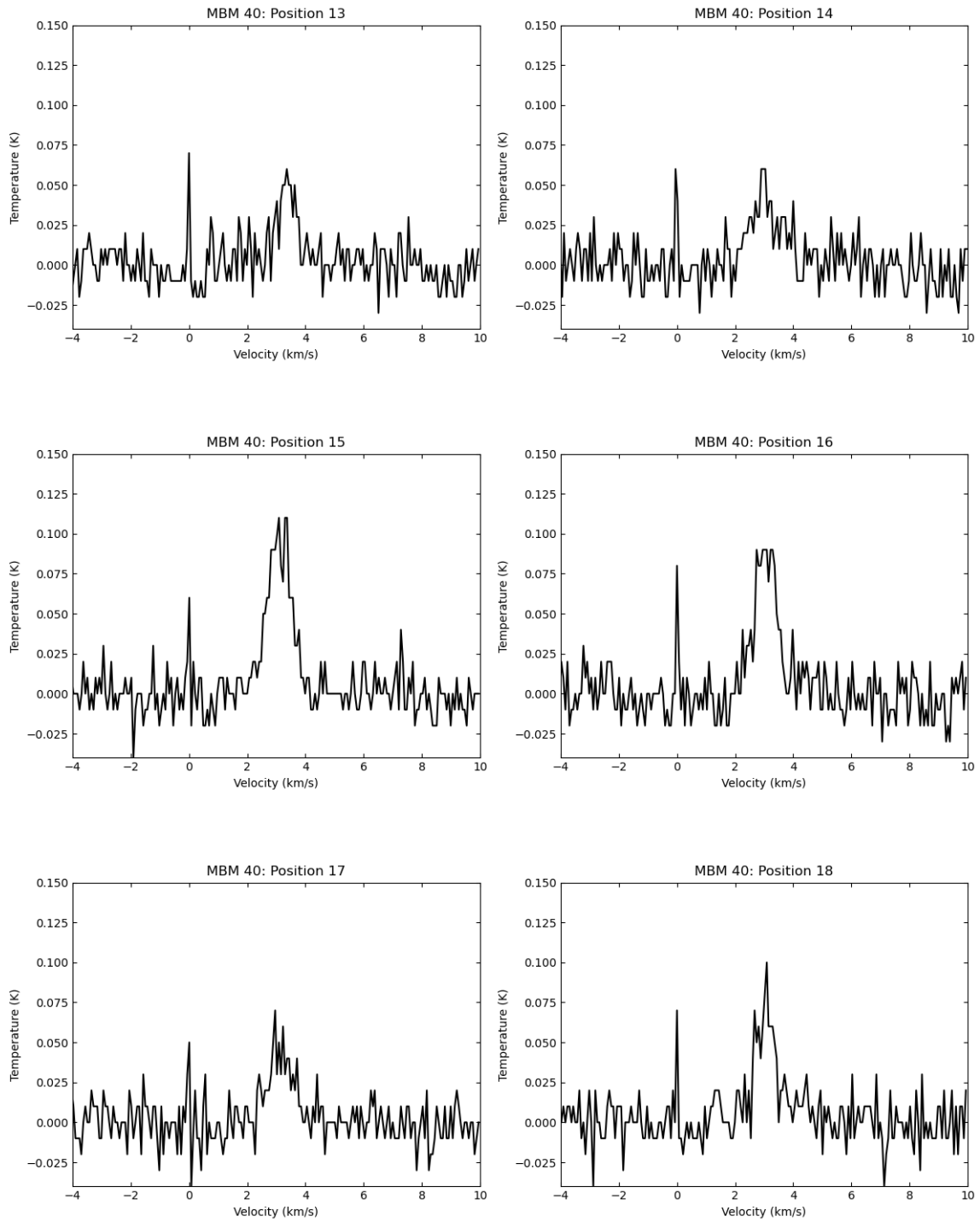


Figure 3.6: MBM 40 CH spectra corresponding to the positions 13-18 in figure 3.3

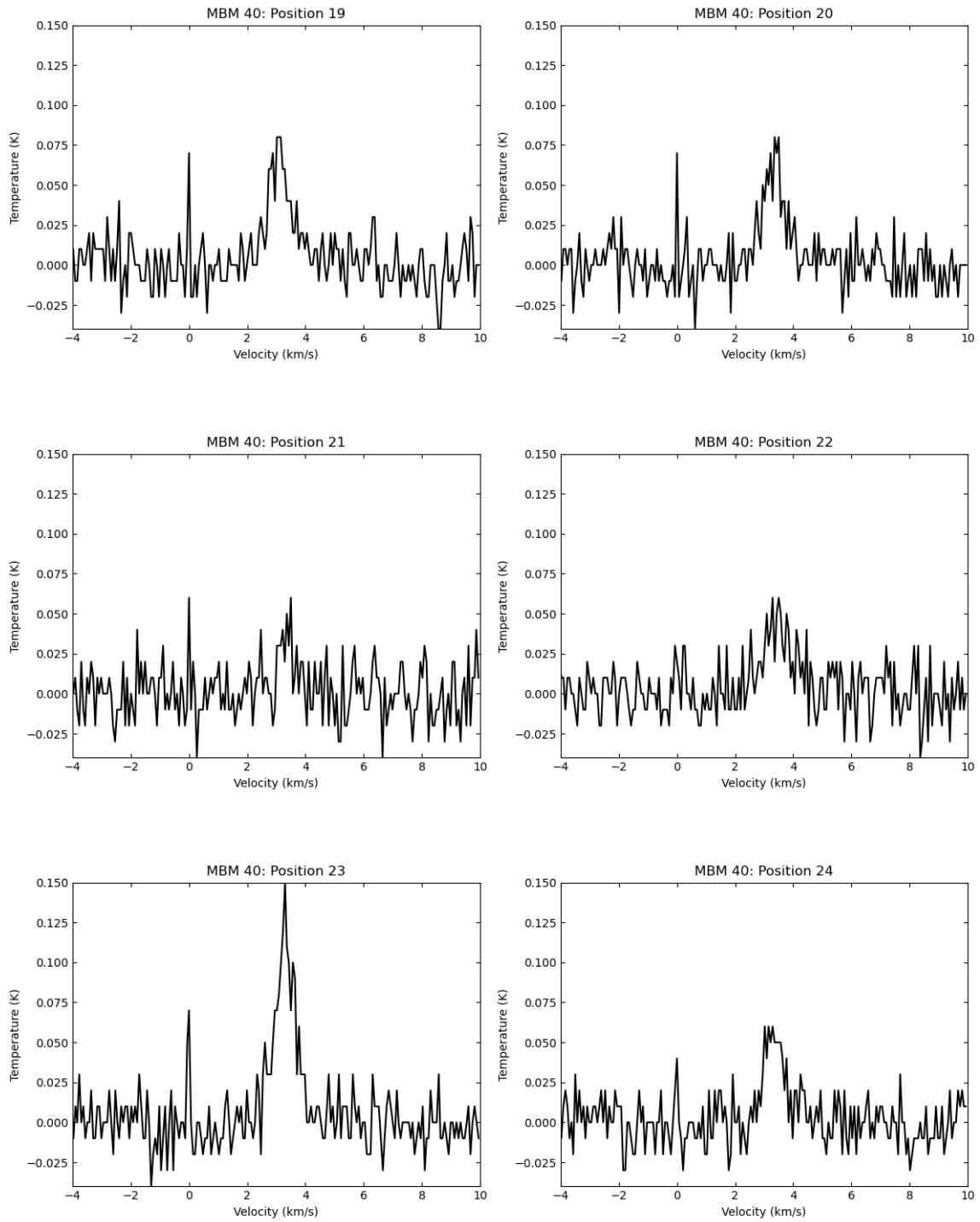


Figure 3.7: MBM 40 CH spectra corresponding to the positions 19-24 in figure 3.3

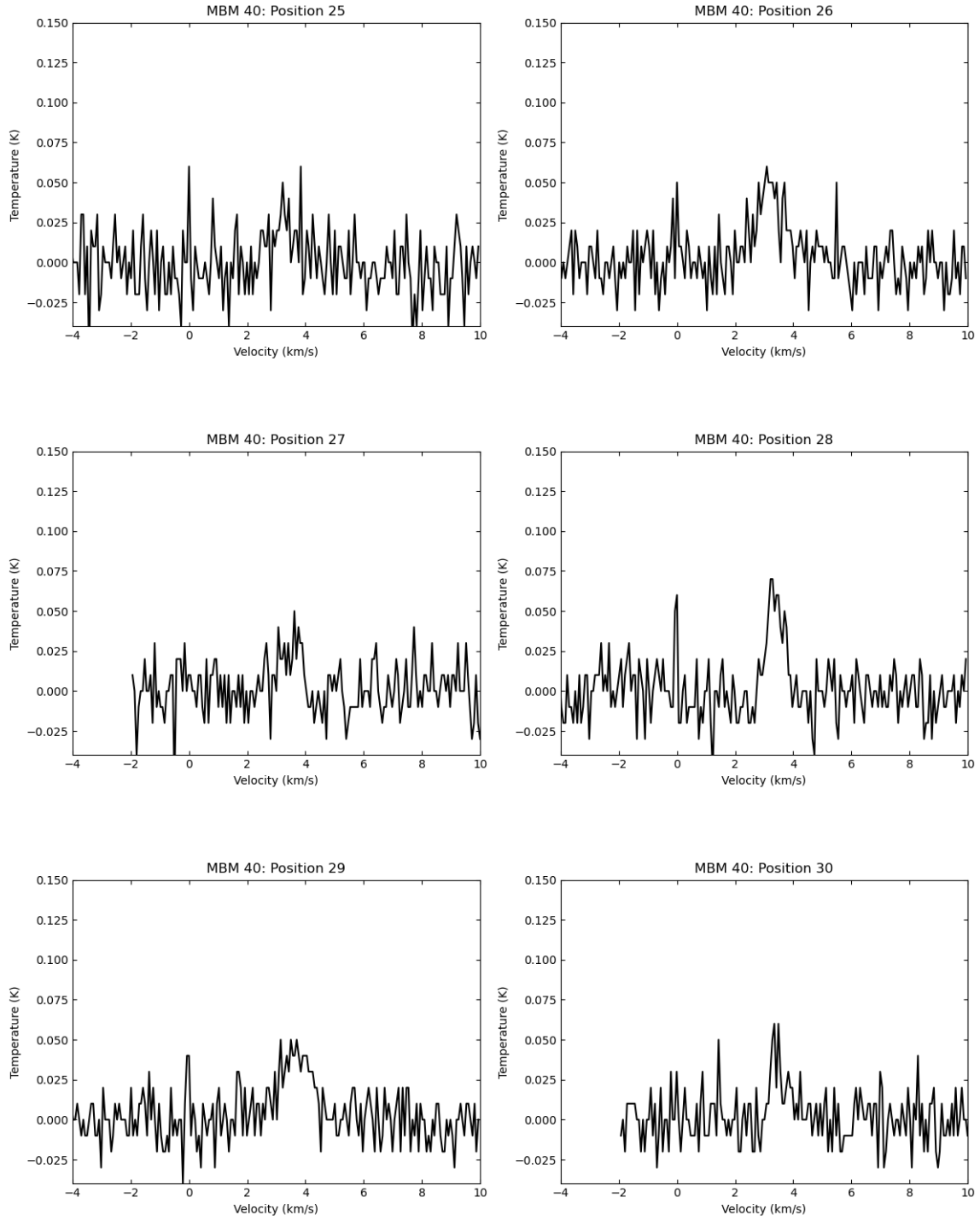


Figure 3.8: MBM 40 CH spectra corresponding to the positions 25-30 in figure 3.3

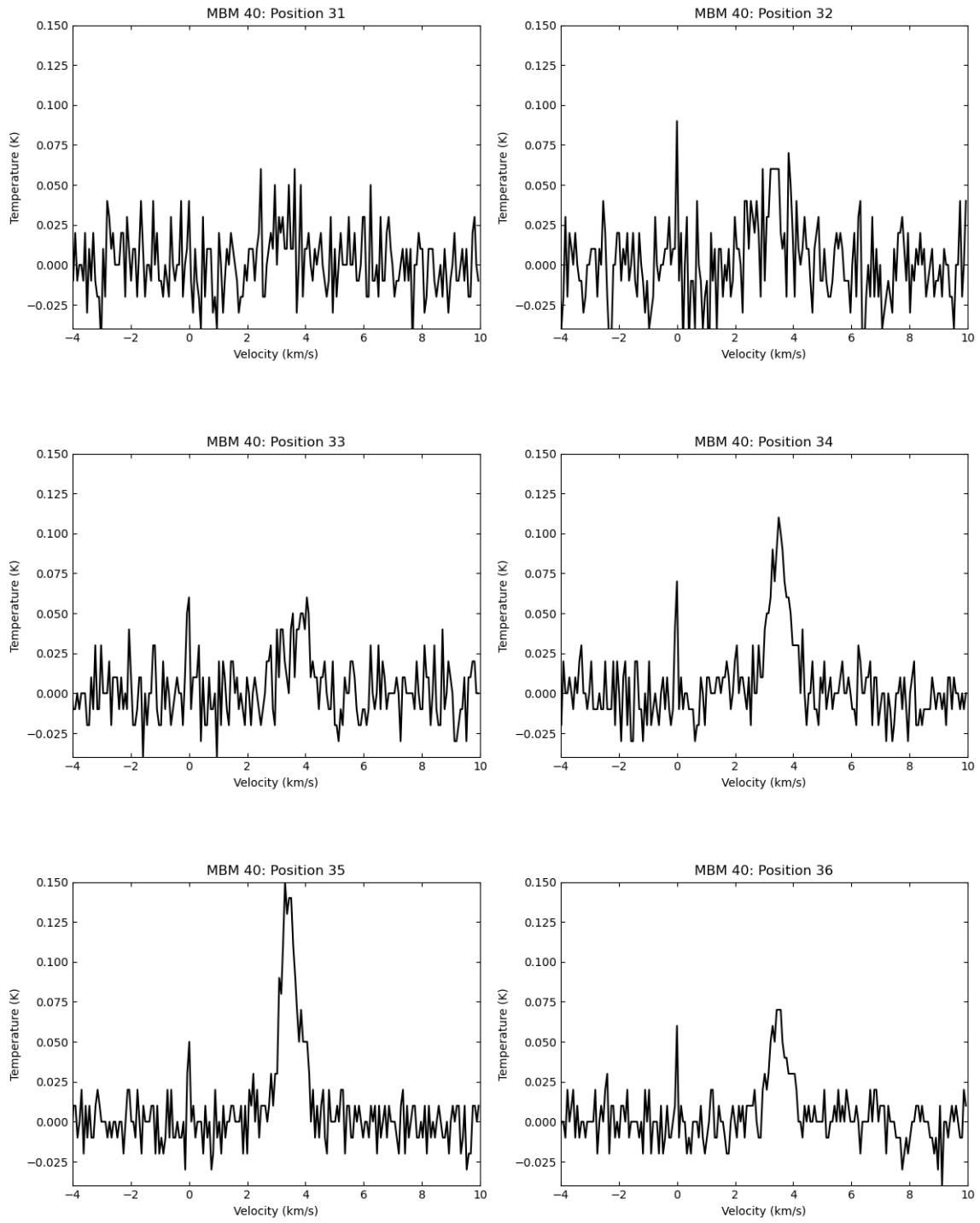


Figure 3.9: MBM 40 CH spectra corresponding to the positions 31-36 in figure 3.3

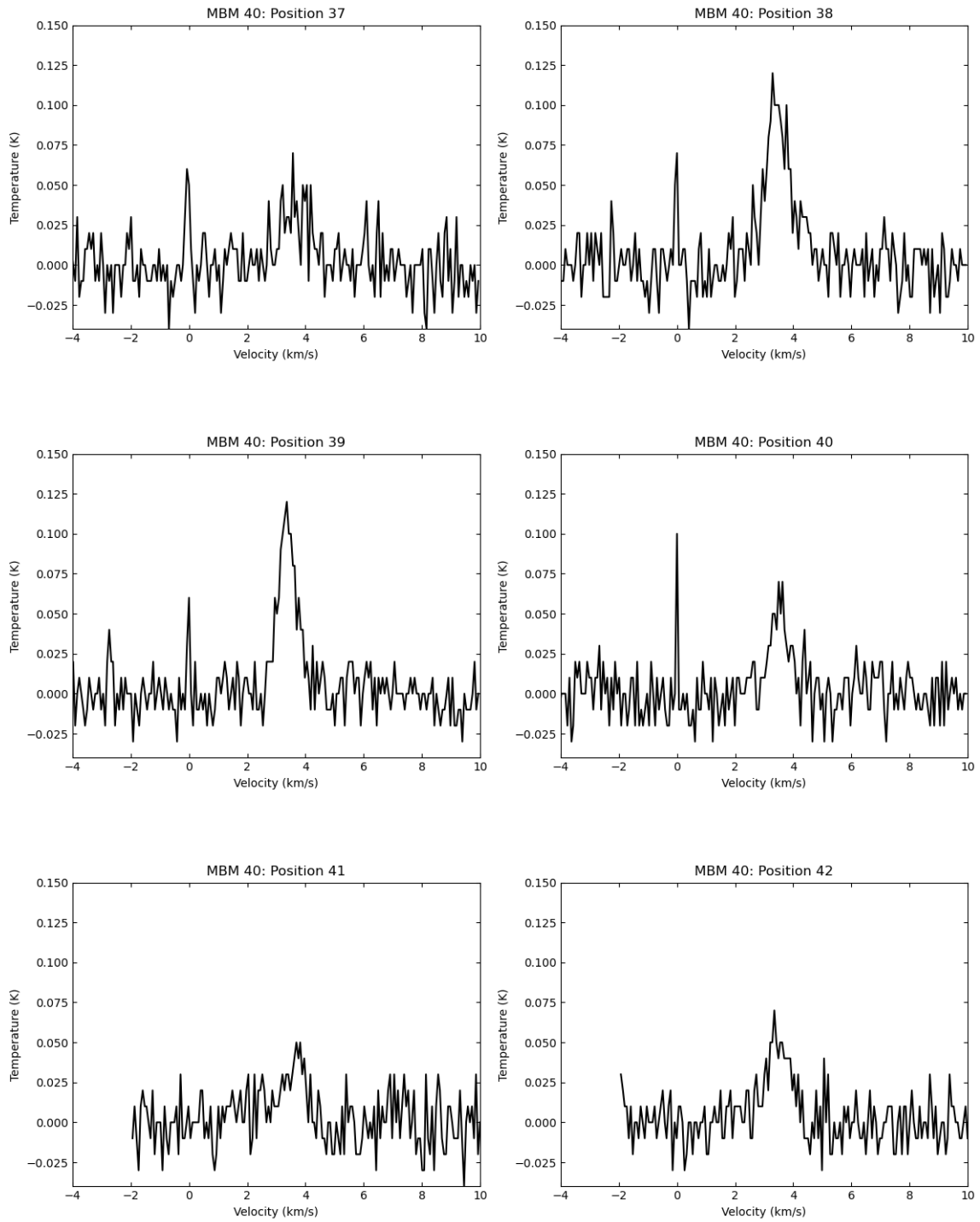


Figure 3.10: MBM 40 CH spectra corresponding to the positions 36-41 in figure 3.3

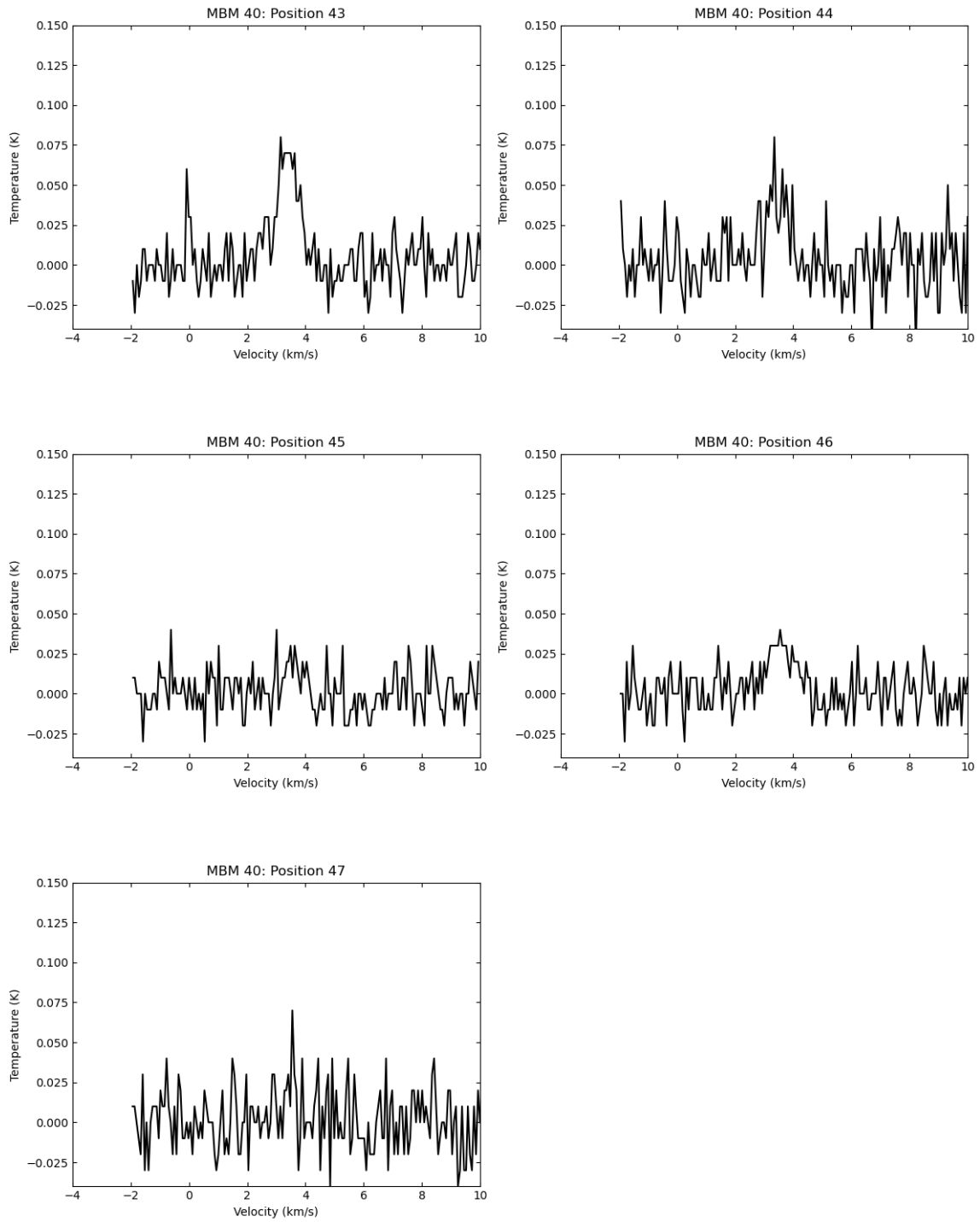


Figure 3.11: MBM 40 CH spectra corresponding to the positions 40-47 in figure 3.3

## CHAPTER 4

### THE CH - E(B-V) RELATION

#### 4.1 INTRODUCTION

In the renowned book “Physical Processes in the Interstellar Medium,” Lyman Spitzer (1978) proposed that the gas-to-dust ratio in the Interstellar Medium was constant over large regions. Since the dust content of a cloud is easier to measure (e.g. via the color excess,  $E(B-V)$ ) than its gas content, observations of dust can be used to estimate the gas column density. *Copernicus* satellite UV absorption line data were used by Savage et al. (1977) and Bohlin, Savage, and Drake (1978) to find a relation between total hydrogen column density based on the total number of hydrogen nucleons ( $N(H_{\text{tot}}) = N(\text{HI}) + 2N(\text{H}_2)$ ) and color excess ( $E(B-V)$ ). They were able to determine  $N(H_{\text{tot}})$  by observing the HI  $L\alpha$  line and the  $\text{H}_2$  J=0 to J=1 vibrational ground state transitions for more than 100 stellar lines of sight. Combining this data with each star’s  $E(B-V)$  value, they derived the well-known relation:

$$\frac{N(H_{\text{tot}})}{E(B - V)} = 5.8 \times 10^{21} \text{ atoms cm}^{-2} \text{ mag}^{-1} \quad (4.1)$$

Diplas and Savage (1994) furthered this work by using IUE observations towards stars with only HI along the line of sight. They found a slope similar to that of Bohlin, Savage, and Drake (1978):  $4.93 \times 10^{21} \text{ atoms cm}^{-2} \text{ mag}^{-1}$  (hereafter, we will drop

the units for simplicity). Rachford et al. (2002) used *FUSE* satellite data to make direct H<sub>2</sub> column density measurements and obtained a slope of  $5.6 \times 10^{21}$ , again similar to the previous values. The differences in  $\frac{N(\text{H}_{\text{tot}})}{E(\text{B-V})}$  were attributed mainly to the stellar samples used in addition to the data being collected by different satellites and spectrometers.

These works are limited due to the lines of sight being along a portion of the galactic plane ending on a stellar surface. A new approach was used by Liszt (2014). He used the dust map derived by Schlegel, Finkbeiner, and Davis (1998) at a resolution of 6' to approximate E(B-V) color excess values for each line of sight. These estimates are for lines of sight extending throughout the Galaxy rather than terminating on a star. Liszt used data from high-resolution (4') and low-resolution (36') 21 cm HI surveys to find the column density of HI (N(HI)). To avoid lines of sight with substantial amounts of molecular gas and atomic hydrogen opacity phenomena, he used lines of sight at  $|b| \geq 20^\circ$  and with  $E(\text{B-V}) \leq 0.1$  mags. By using this markedly different approach, Liszt found a higher value for the  $\frac{N(\text{H}_{\text{tot}})}{E(\text{B-V})}$  ratio:  $8 \times 10^{21}$  but still within a factor of two of the previous work. In summary, these studies found  $\frac{N(\text{H}_2)}{E(\text{B-V})}$  values ranging from  $5\text{-}8 \times 10^{21}$ .

#### 4.2 THE W(CH) - E(B-V) DATA

Using the CH 3335 MHz data, we estimated values for N(H<sub>2</sub>) for each of the positions in our sample described in chapter 3. The spectral line intensity (the velocity-integrated brightness temperature) is used to derive N(CH) which is then converted to N(H<sub>2</sub>) using the measured  $\frac{\text{CH}}{\text{H}_2}$  abundance ( $(4.3 \pm 1.9) \times 10^{-8}$ , see Liszt and Lucas

(2001)). We start by finding the velocity-integrated CH brightness temperature, defined as  $W(\text{CH})$  with units of  $\text{K km s}^{-1}$ .

Each of the summed spectra in figures 3.4-3.11 were fit with a Gaussian profile. Each Gaussian is characterized by a width, the standard deviation,  $\sigma$ , a height (the antenna temperature  $T_A$  which corresponds to the peak intensity), and a velocity centroid ( $v_0$ ). The results are shown in Table 4.1. The antenna temperature can be related to the brightness temperature,  $T_B$ , by the relation  $T_B = \frac{T_A}{\eta_B}$ , where  $\eta_B$  is the beam efficiency of the Arecibo radiotelescope at 3.3 GHz at the time the observations were made. Chastain (2005) estimated  $\eta_B$  to be 0.6 for both observing runs that our data are taken from.

The results of the Gaussian fitting are shown in table 4.1 in addition to  $W(\text{CH})$ . The directly observed quantity,  $W(\text{CH})$ , is the area under the Gaussian profile which is approximated using the values of  $\sigma$  and the peak antenna temperature,  $T_A$  ( $T_A = \frac{T_B}{0.6}$ ), using the formula:

$$W^*(\text{CH}) = 1.07 \times T_A \times 2.35 \times \sigma \quad (4.2)$$

To distinguish between values using  $T_B$  and  $T_A$ , we denote the integrated antenna temperature by  $W^*(\text{CH})$ , and the integrated brightness temperature by  $W(\text{CH})$ . A program was used to find reddening values from the NASA/IPAC Extragalactic Database (NED) Galactic Extinction Calculator<sup>1</sup> for each original position in MBM 40 in figure 3.3. From these values, an average reddening ( $A_V$ ) was found for each summed position in table 4.1. Using the values of  $W^*(\text{CH})$  and  $A_V$  in table 4.1, a plot of  $W^*(\text{CH})$  vs  $A_V$  was created (see figure 4.1).

<sup>1</sup>[https://ned.ipac.caltech.edu/extinction\\_calculator](https://ned.ipac.caltech.edu/extinction_calculator)

Table 4.1: MBM40 CH 3335 MHz Detections and Reddening Values

Position	RA	DEC	$A_V$	$v_0$	$\sigma$	$T_A$	$W^*(CH)$
	(2000)		(mags)	( $\frac{\text{km}}{\text{s}}$ )	( $\frac{\text{km}}{\text{s}}$ )	(K)	( $\frac{\text{K km}}{\text{s}}$ )
1	242.43	22.19	0.4333	2.8304	0.3183	0.0552	0.0442
2	242.51	22.19	0.4538	3.1209	0.3483	0.0592	0.0518
3	242.59	22.19	0.4135	3.2244	0.4370	0.0308	0.0339
4	242.68	22.19	0.3973	3.1879	0.2419	0.0317	0.0193
5	242.77	22.19	0.4100	3.6064	0.7544	0.0366	0.0694
6	242.86	22.19	0.3863	3.2311	0.2778	0.0291	0.0203
7	242.40	22.10	0.4398	2.7124	0.5376	0.0277	0.0375
8	242.48	22.10	0.5565	2.9890	0.3180	0.0959	0.0767
9	242.56	22.10	0.5390	3.0847	0.3422	0.0655	0.0564
10	242.64	22.08	0.5090	3.1098	0.3942	0.0653	0.0647
11	242.72	22.08	0.5175	2.9803	0.4397	0.0590	0.0652
12	242.80	22.10	0.5133	3.3607	0.3584	0.0313	0.0282
13	242.91	22.10	0.4444	3.4039	0.3764	0.0551	0.0521
14	242.42	22.03	0.4857	3.0199	0.5059	0.0433	0.0551
15	242.49	22.02	0.6170	3.1053	0.4077	0.1005	0.1030
16	242.58	22.02	0.6103	3.0496	0.3766	0.0923	0.0874

Continued on next page

Table 4.1: MBM40 CH 3335 MHz Detections and Reddening Values (Continued)

Position	RA	DEC	$A_V$	$v_0$	$\sigma$	$T_A$	$W^*(CH)$
	(2000)		(mags)	$(\frac{km}{s})$	$(\frac{km}{s})$	(K)	$(\frac{K km}{s})$
17	242.66	22.02	0.5110	3.1347	0.4250	0.0462	0.0493
18	242.74	22.02	0.5028	3.0432	0.3590	0.0705	0.0636
19	242.82	22.02	0.5183	3.0582	0.3764	0.0726	0.0687
20	242.91	22.02	0.4945	3.3175	0.3943	0.0663	0.0657
21	242.98	22.01	0.4433	3.3175	0.1882	0.0388	0.0184
22	242.47	21.94	0.5080	3.4557	0.5028	0.0440	0.0557
23	242.54	21.94	0.5873	3.2786	0.3226	0.1211	0.0982
24	242.64	21.93	0.5304	3.3256	0.3472	0.0560	0.0489
25	242.81	21.92	0.4335	3.2743	0.3405	0.0225	0.0192
26	242.99	21.93	0.4367	3.1839	0.4760	0.0473	0.0566
27	242.52	21.86	0.4947	3.4969	0.2535	0.0290	0.0185
28	242.60	21.85	0.5288	3.3889	0.2689	0.0658	0.0445
29	242.68	21.85	0.5105	3.6362	0.5478	0.0433	0.0597
30	242.76	21.83	0.4745	3.0126	0.2229	0.0467	0.0262
31	242.86	21.83	0.4140	3.3607	0.5376	0.0261	0.0352

Continued on next page

Table 4.1: MBM40 CH 3335 MHz Detections and Reddening Values (Continued)

Position	RA	DEC	$A_V$	$v_0$	$\sigma$	$T_A$	$W^*(CH)$
	(2000)		(mags)	$(\frac{\text{km}}{\text{s}})$	$(\frac{\text{km}}{\text{s}})$	(K)	$(\frac{\text{K km}}{\text{s}})$
32	243.03	21.83	0.4055	3.3607	0.4121	0.0435	0.0450
33	242.58	21.78	0.5080	3.8794	0.3584	0.0376	0.0339
34	242.65	21.77	0.5618	3.5195	0.3477	0.0918	0.0803
35	242.73	21.77	0.5635	3.4348	0.3046	0.1344	0.1029
36	242.83	21.77	0.4494	3.5018	0.3302	0.0621	0.0516
37	242.63	21.69	0.5217	3.6368	0.5015	0.0364	0.0459
38	242.70	21.69	0.5573	3.4536	0.4466	0.0961	0.1079
39	242.79	21.69	0.5280	3.3739	0.3202	0.1065	0.0858
40	242.88	21.68	0.4278	3.5336	0.2599	0.0546	0.0357
41	242.68	21.61	0.4913	3.6768	0.3113	0.0326	0.0255
42	242.76	21.60	0.5143	3.4785	0.4253	0.0523	0.0559
43	242.84	21.60	0.4913	3.3833	0.3850	0.0720	0.0697
44	242.90	21.60	0.4375	3.4217	0.3876	0.0464	0.0453
45	242.74	21.53	0.4613	3.6023	0.2623	0.0195	0.0129
46	242.81	21.52	0.4665	3.5603	0.4604	0.0328	0.0380

Continued on next page

Table 4.1: MBM40 CH 3335 MHz Detections and Reddening Values (Continued)

Position	RA	DEC	$A_V$	$v_0$	$\sigma$	$T_A$	$W^*(CH)$
	(2000)		(mags)	( $\frac{\text{km}}{\text{s}}$ )	( $\frac{\text{km}}{\text{s}}$ )	(K)	( $\frac{\text{K km}}{\text{s}}$ )
47	242.87	21.52	0.4545	3.5579	0.0672	0.0565	0.0095

# $W^*(CH)$ vs $A_v$

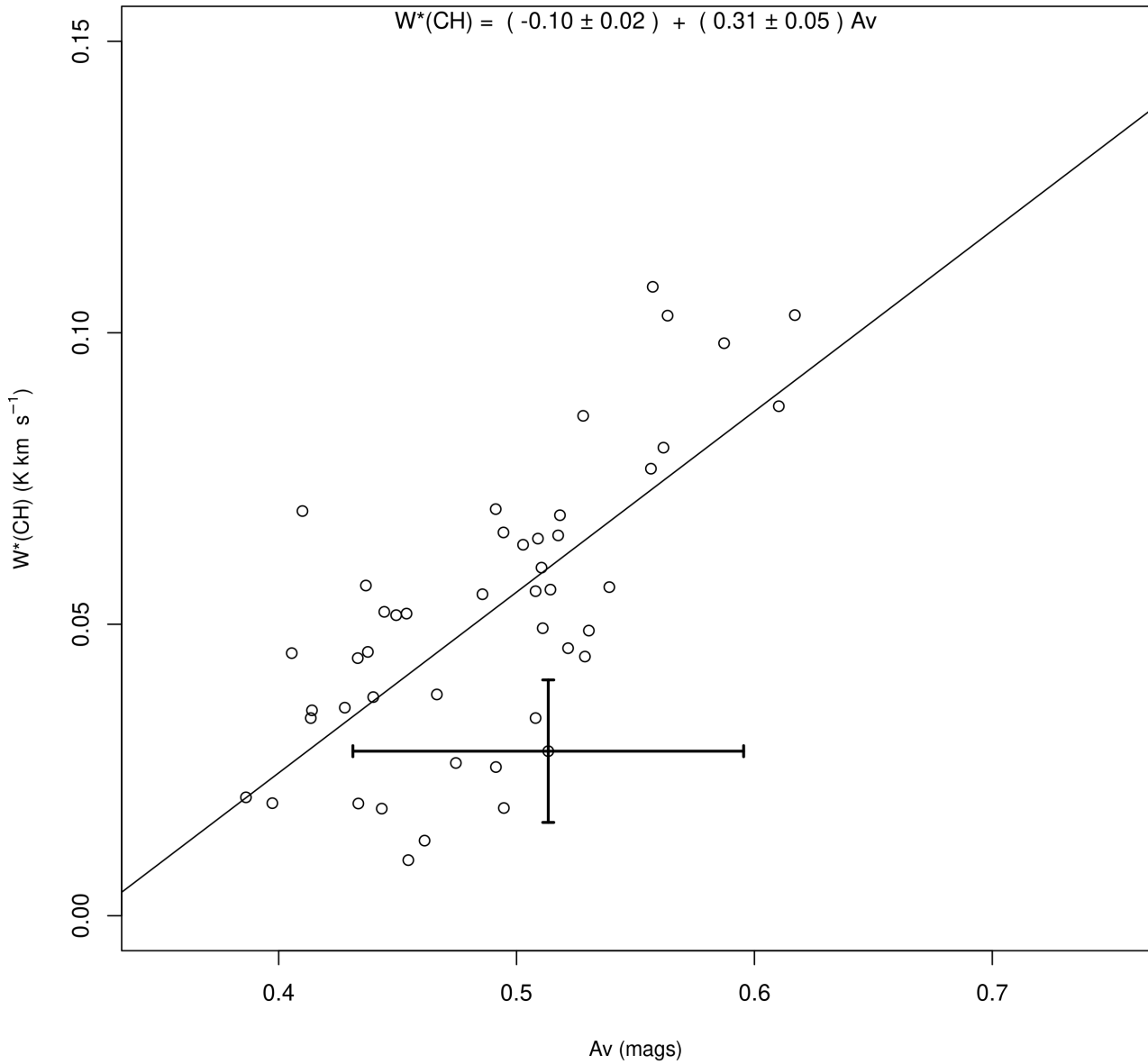


Figure 4.1: Plot of  $W^*(CH)$  (using  $T_A$  instead of  $T_B$ ) as a function of  $A_v$ . The slope of the relation is  $(0.31 \pm 0.05) \text{ K km s}^{-1} \text{ mags}^{-1}$  with a P value of  $4.35 \times 10^{-8}$ . Representative error bars are shown for one of the points.

### 4.3 HOW TO CALCULATE $N(\text{H}_2)$ FROM $W(\text{CH})$

A linear relationship between  $W(\text{CH})$  and  $A_v$  was found in figure 4.1 with a slope of  $0.31 \text{ K km mags}^{-1} \text{ s}^{-1}$ . The visual extinction,  $A_v$ , relates to  $E(\text{B-V})$ , the color excess, by

$$A_v = 3 E(\text{B} - \text{V}) \quad (4.3)$$

(see, e.g. Spitzer 1978). Thus, by dividing the slope in Figure 4.1 by 3, we can associate a value of  $W(\text{CH})$  with a given color excess for all the points in our map of MBM 40. However, the physically relevant quantity is  $N(\text{CH})$  (the column density of CH). We derive  $N(\text{CH})$  from  $W(\text{CH})$  using

$$N(\text{CH}) = 2.82 \times 10^{14} W(\text{CH}) \quad (4.4)$$

This relation is valid for  $T_{\text{ex}} \gg T_{\text{by}}$  (e.g., see Mattila 1986; Magnani and Onello 1995). Using the inverse of the  $\frac{\text{CH}}{\text{H}_2}$  abundance given by Liszt and Lucas (2001) we can find  $N(\text{H}_2)$  with an uncertainty,  $\delta N(\text{H}_2)$ , given by standard error analysis (see Taylor (1997)).

### 4.4 FINDING $N(\text{H}_2)$ THROUGHOUT MBM 40

An  $E(\text{B-V})$  color-excess map of MBM 40 extending  $2^\circ \times 2^\circ$  (clearly encompassing the entirety of the cloud) and consisting of 100 by 100 pixels was made using values from Schlegel, Finkbeiner and Davis (1998) (see figure 4.2). The map's 10,000  $E(\text{B-V})$  values were binned in 0.03 mag intervals and the resulting histogram is shown in figure 4.3. Thus we can use the slope from the plot of  $W(\text{CH})$  vs  $A_v$  in figure 4.1, to determine  $W(\text{CH})$  for each bin.

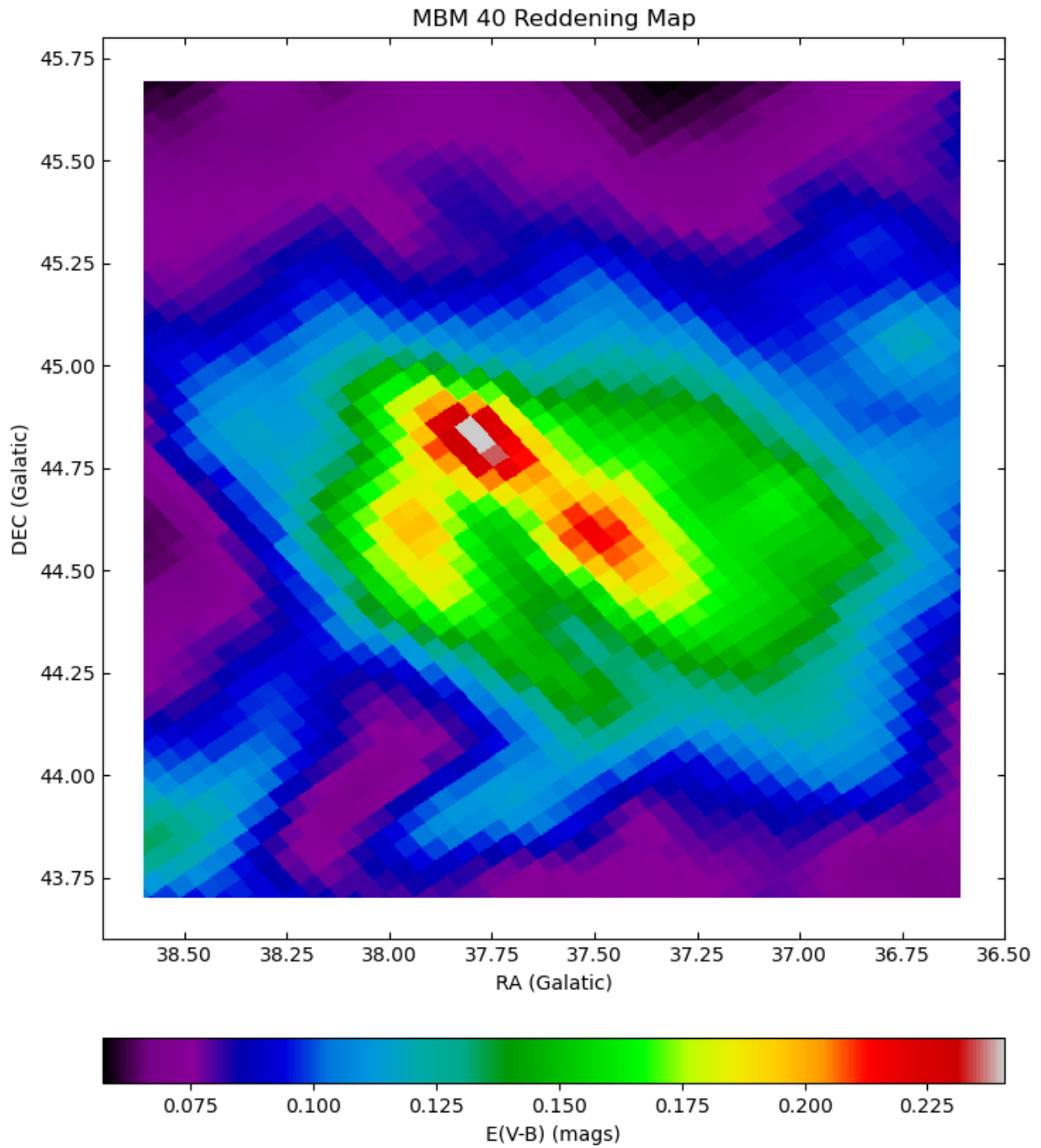


Figure 4.2: A  $2^\circ \times 2^\circ$  reddening map of MBM 40 from Schlegel, Finkbeiner and Davis (1998) using galactic coordinates. The reddening map is 100 by 100 pixels centered at (37.6, 44.7). A color excess value ( $E(V-B)$ ) at each point in the map corresponds to a value on the colorbar.

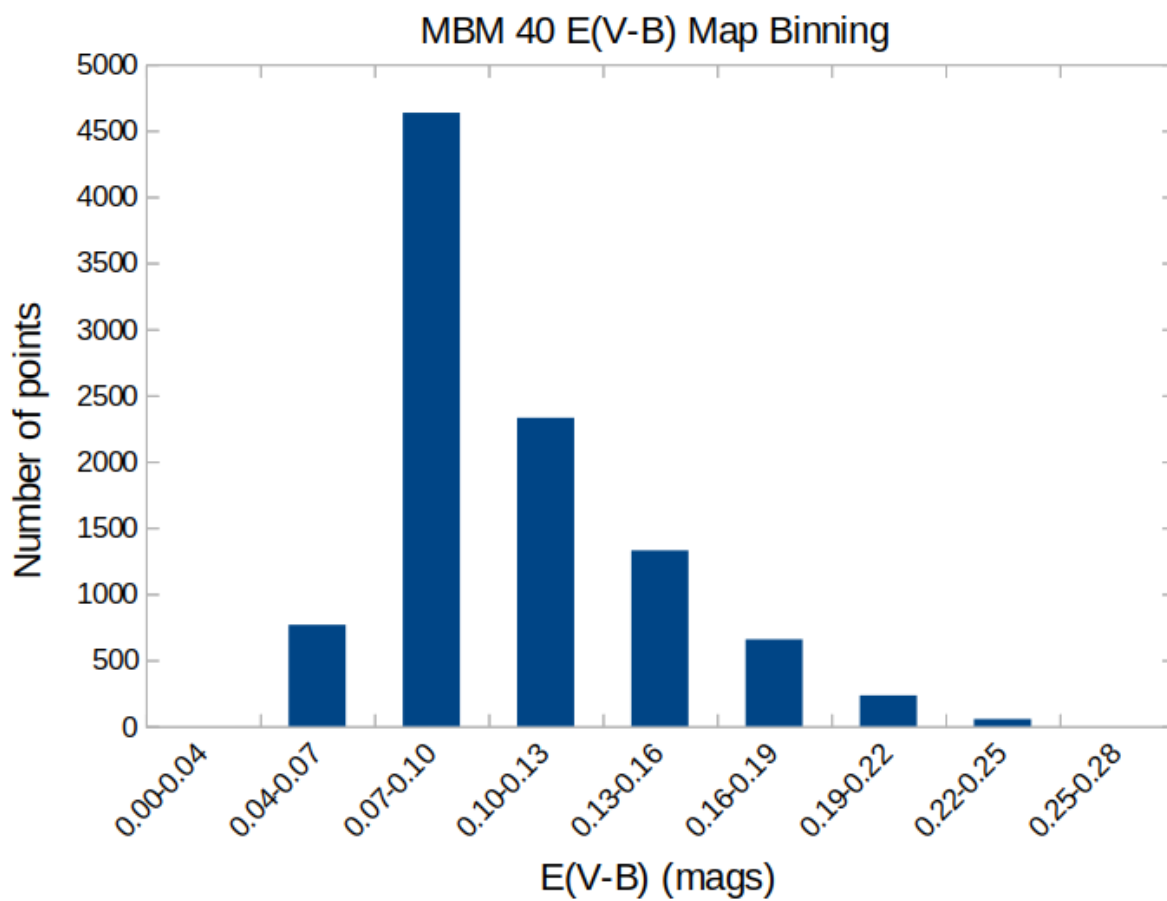


Figure 4.3: Bins corresponding to E(V-B) values in MBM 40 from the color excess map in figure 4.2

#### 4.5 THE MOLECULAR EXTENT OF MBM 40

As previously discussed, the strongest CO(1-0) emission in MBM 40 comes from an arc-like molecular structure which is surrounded by a lower density molecular envelope (see Cotten and Magnani 2013). Cotten et al. (2012) used OH 18 cm data to find a similar result. A bigger HI “cocoon” encircles the arc-like molecular structure; the latter might be a small component of an extended atomic hydrogen shear flow (Shore et al., 2003); a portion of this HI flow kinks or bends into the arc-like structure and becomes molecular perhaps through a thermal instability.

MBM 40 color excess values in figure 4.2 are measured from dust emissions associated with either the molecular gas or a surrounding atomic component. Although it is difficult to distinguish between these dust components, it is evident that the lower E(B-V) values emanate from dust associated only with the atomic component.

A E(B-V) cutoff must be determined to distinguish between dust emissions arising from atomic components and those arising from molecular components of the structure of MBM 40. We’ll apply two fundamental principles to decide where the cutoff is found:

- 1) Across MBM 40, the mean value of N(HI) is  $3.9 \times 10^{20} \text{ cm}^{-2}$  (Gir, Blitz, and Magnani 1994). This average value of N(HI) corresponds to the bin with E(B-V) values 0.05 to 0.08 when we use the  $\frac{N(\text{H}_{\text{tot}})}{E(\text{B-V})}$  ratios ( $5 - 8 \times 10^{21}$ ) from section 4.1.
- 2) Our data’s lowest W(CH) values were found at  $A_V \sim 0.4$  mags or, equivalently,  $E(\text{B} - \text{V}) \sim 0.13$  (see figure 4.1). Considering that these two values are estimates for the lowest E(B-V) values corresponding to molecular emission, we select the bin E(B-V) values in the bin ranging from 0.10-0.13 mags as the lowest range which arises

mainly from dust associated with molecular gas. Thus, 4,600 of figure 4.1's 10,000 pixels are in bins with values of  $E(B-V) > 0.10$  mags. Since the figure spans  $2^\circ \times 2^\circ$ , we estimate the total solid angle which has dust that corresponds to detectable molecular emission that our sensitive CH observations can detect is 1.84 square degrees. We will use the solid angle calculated from each bin with a color excess range greater than or equal to 0.10-0.13 in our mass computation in chapter 5.

#### 4.6 ERROR ANALYSIS INCLUDING THE $\frac{W(CH)}{E(B-V)}$ RELATION

Since our method for determining mass uses the ratio  $\frac{W(CH)}{E(B-V)}$  which is derived in section 4.2, we include the uncertainty of the slope of the best fit line from figure 4.1. We begin with determining  $\delta W^*(CH)$  including the uncertainty in the slope. The uncertainty in this calculation,  $\delta W^*(CH)$ , is given by (Taylor 1997):

$$\delta W^*(CH) = \left( \sqrt{\left( \frac{\delta E(V-B)}{E(V-B)} \right)^2 + \left( \frac{\delta \text{slope}}{\text{slope}} \right)^2} \right) W^*(CH) \quad (4.5)$$

where  $\delta E(V-B)$  is the error in the color excess values which is about 16% of each  $E(V-B)$  value (Schlegel, Finkbeiner and Davis (1998)). Using equations 4.2, 4.4, and 4.5, we find the corresponding  $W(CH)$  values and their uncertainties,  $\delta W(CH)$ , at each point in the MBM 40 color map in figure 4.2. Using equation 4.2 for the CH column density,  $N(CH)$ , produces an uncertainty  $\delta N(CH)$  which can be expressed as

$$\delta N(CH) = 2.82 \times 10^{14} \delta W(CH) \quad (4.6)$$

The new uncertainties are tabulated in table 4.2. We will use these values to determine the mass of MBM 40 in chapter 5.

E(B-V)	N	W(CH)	$\delta$ W(CH)	N(CH)	$\delta$ N(CH)	N(H2)	$\delta$ N(H2)
0.00-0.04	0	0.019	0.004	5.25E+12	1.16E+12	1.22E+20	6.03E+19
0.04-0.07	766	0.051	0.011	1.44E+13	3.18E+12	3.36E+20	1.66E+20
0.07-0.10	4634	0.079	0.017	2.23E+13	4.92E+12	5.19E+20	2.56E+20
0.10-0.13	2330	0.107	0.024	3.02E+13	6.66E+12	7.02E+20	3.47E+20
0.13-0.16	1328	0.135	0.03	3.80E+13	8.39E+12	8.85E+20	4.37E+20
0.16-0.19	656	0.163	0.036	4.59E+13	1.01E+13	1.07E+21	5.27E+20
0.19-0.22	232	0.191	0.042	5.38E+13	1.19E+13	1.25E+21	6.18E+20
0.22-0.25	54	0.219	0.048	6.17E+13	1.36E+13	1.43E+21	7.08E+20
0.25-0.28	0	0.247	0.054	6.95E+13	1.53E+13	1.62E+21	7.99E+20

Table 4.2: Tabulated data derived from the reddening map of MBM 40 in figure 4.2. The color excess values at each point are placed into bins spanning a color excess range with a total number of points in each bin is given by variable N. The triple underline denotes the boundary between the color excess bins which correspond to the lowest-density molecular component of MBM 40 and those that are likely to be mostly atomic.

## CHAPTER 5

### THE MASS OF MBM 40 FROM SENSITIVE CH OBSERVATIONS.

#### 5.1 DETERMINATION OF CLOUD MASS

The mass of a molecular region can be estimated by the relation:

$$M = \overline{N(H_2)} \Omega d^2 \mu m_H \quad (5.1)$$

where  $\overline{N(H_2)}$  is the average column density of molecular hydrogen in that region,  $\Omega$  is the solid angle that the cloud covers (1.84 square degrees or  $5.6 \times 10^{-4}$  steradians for MBM 40 - see Chapter 4),  $d$  is distance,  $\mu$  is the mean molecular weight which has a value of 2.3 including the contribution from helium, and  $m_H$  is the mass of hydrogen. Rather than using an average of  $N(H_2)$  for the entire cloud, we calculate the mass in each E(B-V) bin (see Chapter 4). This allows a more thorough consideration for the cloud structure. The solid angle in each E(B-V) bin is determined from our  $2^\circ \times 2^\circ$  map and expressed in steradians as:

$$\Omega_i = 4 n_i N^{-1} (2\pi (360)^{-1})^2 \quad (5.2)$$

where  $n_i$  is the total number of pixels in a bin and  $N$  is the total number of pixels in the E(V-B) map of MBM 40 in total (i.e., 10,000). The 4 represents the  $2^\circ \times 2^\circ$  region that we analyzed. Thus, the product  $n_i N^{-1}$  represents the fraction of the

$2^\circ \times 2^\circ$  region at a given E(B-V). The two most significant sources of uncertainty in the mass determination are from the distance and from the column density (as determined in Chapter 4). Since the distance is squared in equation 5.1, we derive the uncertainty in the mass using the general rule for uncertainties (e.g., see Taylor 1997 page 75):

$$\begin{aligned} \delta M &= \sqrt{\left(\frac{\partial M}{\partial d} \delta d\right)^2 + \left(\frac{\partial M}{\partial N(\text{H}_2)} \delta N(\text{H}_2)\right)^2} \\ &= M \sqrt{\left(\frac{2\delta d}{d}\right)^2 + \left(\frac{\delta N(\text{H}_2)}{N(\text{H}_2)}\right)^2} \end{aligned} \tag{5.3}$$

The distance to MBM 40 and its uncertainty were determined by Zucker et al. 2019 ( $d = (93 \pm 22)$  pc). The estimated area for the molecular portion of the cloud was 1.84 square degrees based on an E(B-V) cutoff of 0.1 mag for regions with significant molecular gas. We tabulate our results for the mass in each E(B-V) bin in Table 5.1. If we total the mass from all the bins at  $E(B - V) \geq 0.10$ , we derive a molecular cloud mass for MBM 40 of  $44 M_\odot \pm 22 M_\odot$  which is a lower limit. It could be argued that bin 0.10-0.13 should also be included, but we chose the most conservative option.

E(V-B) Range	M(H <sub>2</sub> ) (Kg)	$\delta$ M(H <sub>2</sub> ) (Kg)	Mass (M <sub>⊙</sub> )	$\delta$ M(H <sub>2</sub> )(M <sub>⊙</sub> )
0.00-0.04	0	0	0.00	0.00
0.04-0.07	9.94E+30	4.91E+30	5.00	2.47
0.07-0.10	9.29E+31	4.59E+31	46.71	23.07
0.10-0.13	6.32E+31	3.12E+31	31.78	15.69
0.13-0.16	4.54E+31	2.24E+31	22.84	11.28
0.16-0.19	2.71E+31	1.34E+31	13.61	6.72
0.19-0.22	1.12E+31	5.54E+30	5.64	2.79
0.22-0.25	2.99E+30	1.48E+30	1.50	0.74
0.25-0.28	0	0	0.00	0.00

Table 5.1: Color excess range and associated masses. The triple underline denotes the color excess range which corresponds to the lowest-density molecular component of MBM 40.

## 5.2 DISCUSSION

Our value for the mass of MBM 40 as derived from sensitive CH observations is  $44 M_{\odot} \pm 22 M_{\odot}$ . Previous estimates for the cloud mass are as follows: Cotten et al. (2012) used OH observations at 18 cm over the southern portion of MBM 40 to determine a mass in the core, envelope, and periphery of the cloud of  $4 M_{\odot}$ ,  $8 M_{\odot}$ , and  $5 M_{\odot}$ , respectively. Their core region corresponds to the arc-like region in figure 3.1, and the envelope and the periphery correspond to the inner portion “cocoon” surrounding the arc-like region while the periphery is an outer part of the cocoon. Their total mass in the three regions of  $17 M_{\odot}$  is clearly less than our value. An earlier study by Magnani et al. (1996) estimated the mass of MBM 40 from CO and IRAS data to the  $20\text{-}40 M_{\odot}$  with  $\sim 20 M_{\odot}$  in the molecular ridge (equivalent to

our arc-like region). Nevertheless, because this study did not sufficiently sample the regions outside the arc-like, densest portion of the cloud, it must only be considered as an approximation. Their upper most range is consistent with our estimate. Lastly, Chastain (2005) determined the molecular mass of the arc-like structure in MBM 40 to be  $\sim 21 M_{\odot}$  using the same data as used in this thesis but at half the sensitivity. At that sensitivity, Chastain did not detect any CH emission beyond the arc-like structure. Although Chastain (2005) did not present an uncertainty in his estimate for the molecular mass of MBM 40, we can assume that the estimate has an implied uncertainty of at least  $\sim 1 M_{\odot}$ . With this assumption, our mass estimate agrees with that of MBM 40 within  $1 - \sigma$  and assuming a normal distribution of solar masses with the mean being  $44 M_{\odot}$  and a standard deviation of  $22 M_{\odot}$ , we have an 84% chance of our measurement being greater than that of (2005). Thus we can say that our measured mass estimate is an improvement and that we detected more molecular gas. We note here, as we did in chapter 3, that by summing over nearby regions, we detected CH in all our spectra, whereas Chastain (2005) detected CH emission in 88 out of 164 positions.

## CHAPTER 6

### CONCLUSIONS

In this thesis, we summed archival CH spectra for the cloud MBM 40 from adjacent lines of sight in an effort to improve the rms and thus the sensitivity of the original observations. This was done in an effort to determine whether or not the 3335 MHz CH emission line could be an effective tracer of low-density molecular gas at the edges of small, diffuse molecular clouds.

Averaging several spectra from nearby regions resulted in a rms reduced by a factor of 2 from the original work that the data were taken for (Chastain 2005) and CH emission was detected at each summed position (47 out of 47), a significant improvement from Chastain (2005) who detected CH from 88 out of 164 positions.

The preceding result shows that the CH 3335 MHz transition emission line is an effectual tracer of low-density molecular gas in diffuse and translucent molecular clouds. The mass estimate for the whole cloud is  $44 \pm 22 M_{\odot}$ , which is about a factor of 2 more than what has been calculated using CO and OH. It is likely that this extra mass could be identified as the so-called “dark molecular gas” found by Grenier et al. (2005). In conclusion, sensitive CH observations at 3335 MHz are most likely associated with at least some of the lowest-density molecular gas identifiable in diffuse clouds and, as such, are an excellent way of tracing this component.

## BIBLIOGRAPHY

- Bohlin, R.C., Savage, B.D., and Drake, J.F. 1978, 224, 132
- Chastain, R.J. 2005, Ph.D. thesis, University of Georgia
- Chastain, R.J., Cotten, D., and Magnani, L. 2009, AJ, 139, 267
- Cotten, D.L., Magnani, L., Wennerstrom, E.A., Douglas, K.A., and Onello, J.S. 2012, AJ, 144, 163
- Cotten, D.L., and Magnani, L. 2013, MNRAS, 436, 1152
- Cox, P., Güsten, R., & Henkel, C. 1988, A&A, 206, 108
- Diplas, A. and Savage, B.D. 1994, ApJ, 427, 274
- Donate, E. and Magnani, L. 2017, MNRAS, 472, 3169
- Donate, E., White, J., and Magnani, L. 2019, MNRAS, 486, 4414
- Federman, S.R. and Willson, R.F. 1984, ApJ, 283, 626
- Gir, B.-Y., Blitz, L., and Magnani, L. 1994, ApJ, 434, 162
- Goldsmith, P., Baker, L.A., Davis, M.M., and Giovanelli, R. 1995, ASP Conference Series, Vol. 75, D.T. Emerson and J.M. Payne, eds

- Grenier, I.A., Casandjian, J.-M., and Terrier, R. 2005, *Science*, 307, 1292 (GCT)
- Hartquist, T.W., Flower, D.R., and Pineau des Forêts, G. 1990, *Molecular Astrophysics*, ed. T.W. Hartquist, Cambridge U. Press, 99
- Heyer, M. and Dame, T.M. 2015, *A&A*, 53, 583
- Johansson, L.E.B. 1979, *Research Lab. Electronics and Onsala Space Obs. Research Rep. 136* (Onsala: Onsala Space Obs.)
- Liszt, H. and Lucas, R. 2001, *A&A*, 370, 576
- Liszt, H. 2014, *ApJ*, 783, 17
- Magnani, L. 1993, *PASP*, 105(690), 894
- Magnani, L. et al. 1996, *ApJ*, 465, 825
- Magnani, L et al. 1998, *ApJ*, 504, 290
- Magnani, L. and Onello, J.S. 1993, *ApJ*, 408, 559
- Magnani, L. and Onello, J.S. 1995, *ApJ*, 443, 169
- Magnani and Shore 2017, *A Dirty Window: Diffuse and Translucent Molecular Gas in the Interstellar Medium*, GmbH Germany, Springer-Verlag
- Mattila K., 1986, *A&A*, 160, 157
- Peng, R.S., Whiteoak, J.B., Reynolds, J.E., Kuiper, T.B.H., and Peters, W.L. 1992, *PASA*, 10, 113

- Rachford, B.L. et al. 2002, *ApJ*, 577, 221
- Sandell, G., Stevens, M.A., and Heiles, C. 1987, *A&A*, 179, 255
- Savage, B.D., Bohlin, R.C., Drake, J.F., and Budich, W. 1977, *ApJ*, 216, 291
- Schlegel, D.J., Finkbeiner, D.P., and Davis, M. 1998, *ApJ*, 500, 525
- Spitzer, L. 1978, *Physical Processes in the Interstellar Medium*, New York: Wiley
- Taylor, J.R. 1997, *An Introduction to Error Analysis 2nd ed.*, University Science Books
- Wolfire, M.G., Hollenbach, D., and McKee, C.F. 2010, *ApJ*, 716, 1191
- Zucker, C., Speagle, J.S., Schlafly, E.F., Green, G.M., Finkbeiner, D.P., Goodman, A.A., and Alves, J. 2019, *ApJ*, 879, 125